Electrochimica Acta 405 (2022) 139804

Contents lists available at ScienceDirect

Electrochimica Acta

journal homepage: www.elsevier.com/locate/electacta

Bottom-up characterization of electrochemical passivity from simple binary alloys to high entropy alloys

Dominik Dworschak[a], Ko-Kai Tseng[b], Jien-Wei Yeh[b,c], Hsiu-Wei Cheng[d,*], Markus Valtiner[a]

[a] Institute of Applied Physics, Vienna University of Technology, Vienna, 1040, Austria
[b] Department of Materials Science and Engineering, National Tsing Hua University, Hsinchu, 30013, Taiwan
[c] High Entropy Materials Center, National Tsing Hua University, Hsinchu 30013, Taiwan
[d] Department of Chemistry, National Taiwan University, Taipei 10617, Taiwan

ARTICLE INFO

Article history:
Received 10 September 2021
Revised 8 December 2021
Accepted 27 December 2021
Available online 30 December 2021

ABSTRACT

Multi-principal element alloys (MPEAs) are an emerging class of metallic alloys with the capability of customized unique material properties. A high corrosion resistance is an intended characteristic for structural alloys, which usually is achieved by the addition of e.g. Cr. For MPEAs the interplay of alloying elements on the corrosion resistance of the resulting material is less clear. Here we demonstrate a bottom-up systematic approach to study the electrochemical activity of a library of alloys spanning from equimolar binary alloys up to the High Entropy Alloy (HEA) NiCoCrFeMn. Using this approach we can show that chromium oxide does not form an effective passive film at potentials over +0.75 V, where Fe replaces Cr as passivation element. Further, Cr does not generally result in a stable passive film, addition of Mn can significantly weaken the passivity. This and our approach provides useful insight for developing new MPEAs with simultaneously tailored corrosion resistance and mechanical properties.

Introduction

Fundamental metal-metal interactions govern physics, chemical reactions as well as mechanical performance of alloys. Properties of alloys/metal oxides can be tailored towards specific applications by using an increasing number of functional elements and tuning their composition. Newly emerged material classes as high entropy alloys (HEAs) [1–3], high entropy oxides (HEOs) [4–6] and superconductors [7] provide a variety of such possibilities. However, the drastic growth of material complexity creates new problems for design engineering, where the overall material behaviour is simply not a linear superposition of individual compositing elements [8].

In many alloy design strategies, corrosion resistance under extreme environments is a highly desirable property in a wide range of applications that is usually achieved by the addition of e.g. Cr. A critical concentration of Cr in an alloy is believed to be the key to reinforce the corrosion resistance of the alloy. It is suggested that more than 5% of Cr content is needed in an alloy to be highly corrosion-resistant, such as for nickel-based alloys (NBAs) [9–12].

However this general rule seems to be only valid for conventional alloys with the simple composition of one main and several co-alloyed minor components, such as NBAs or stainless steels. For more complex materials like multi-principal element alloys (MPEAs) and high entropy alloys (HEAs), the corrosion resistance built up by Cr might not be correlated to its stoichiometry anymore. Particularly, this effect gets even more pronounced when looking at HEAs, where more than five principal components come in play [13].

NiCoCrFeMn, as an example, is a well-known HEA containing Ni, Cr and Fe similar to NBAs or stainless steels. Based on the experience with NBAs, a 20% Cr content as in NiCoCrFeMn should provide considerable corrosion resistance. Addition of Co and Mn can further provide flexibility in tuning the mechanical performance [14] as well as its electric conductivity [15]. However, it has been shown that the corrosion resistance of NiCoCrFeMn deviates from the prediction. It is considerably deteriorated compared to 304 stainless steel in aqueous 3.5 wt.% NaCl, even though the Cr content is higher [16,17]. This observation indicates the passivity constructed from Cr is weakened by other added principal metals. Therefore, it is crucial to understand the electrochemical correlation across different alloyed functional elements.

The addition of single elements to an otherwise static system is done in a series of studies: Mn has been shown to have a deleterious effect on similar HEAs by a recent study of Panindre et al. [18].

* Corresponding author at: Department of Chemistry, National Taiwan University, Taipei 10617, Taiwan
E-mail addresses: jwyeh@mx.nthu.edu.tw (J.-W. Yeh), williamcheng@ntu.edu.tw (H.-W. Cheng), valtiner@iap.tuwien.ac.at (M. Valtiner).

https://doi.org/10.1016/j.electacta.2021.139804
0013-4686/

Increasing the concentrations of Co has been shown to improve passivity and lower the corrosion rate of Mn-containing steels in sulfuric acid [19]. These findings point out that the alloy composition and the consequential passive film is more critical than the amount of added Cr to its corrosion properties. Generally speaking, the concepts of passivity constructed by single functional elements are valid for simple alloys, but may not be directly applied to MPEAs [20].

To decipher the influence of single alloyed elements as well as the synergy of combination on the electrochemical performance of MPEAs - in our case the corrosion resistance - a material library is capable of providing a large spectrum of property change of different combinations [21,22].

In this work, we designed a bottom-up approach with studying the electrochemical activity starting from simple equimolar binary nickel based alloys NiCo, NiMn, NiCr and NiFe to step-by-step constructing three (NiCoFe, NiCoCr, NiCoMn, NiCrFe, NiCrMn, NiMnFe), four (NiCoCrFe, NiCoCrMn, NiCoFeMn) element mixing and eventually the five element mixed HEA (NiCoCrFeMn). This series allows us to break down the contribution of individual elements to the passivity of the alloys.

To access the single element contribution on the stability of the alloys, ICP-MS is employed, a technique that is capable to elementally resolve the released materials from the alloys. We use a home-designed electrochemical flow cell [23] coupled with downstream ICP-MS detection. A schematic of the used setup can be found in the supporting information Fig.

We use normal pulse voltammetry (NPV) to potential-dependent probe the degradation of alloys. NPV is, in contrast to other electrochemical techniques like linear sweep voltammetry (LSV), more precise in testing anodic oxidation potential-resolved, since the single step potentials are probed individually. On the contrary, for LSV with its constantly changing potential, the 'history' has a much higher impact, since the degradation products and formed passive layers of all applied potentials accumulate on the surface. The reducing of the formed passive film at the base potential between the steps on one hand reconditions the surface to some extent, and on the other hand can provide additional information on the surface chemistry.

Results

Normal pulse voltammetry characterization: As indicated in Fig. 1, the alloys were polarized starting from -0.5 V vs. Ag|AgCl with a step-wise ascending pulse profile with 30 s pulse length (all profiles are shown in Supporting Information Fig.). Depending on the applied voltages, the jump of potential may be accompanied by dissolution of material, with the online flow-cell ICP-MS detection elementally resolving the dissolution current.

At low applied pulse potentials the surface indicates no significant dissolution of material (see left part of Fig. 1). With progressively increasing the step polarization over an alloy- and element-dependent threshold, the dissolution profiles exhibit an increase of dissolution current (middle part of Fig. 1). In general, jumping back to the base potential instantly stops the dissolution. The subsequently observed decay of the dissolution profile results from the diffusion broadening in the flow system [24].

For quantitative analysis the dissolution per step was integrated as indicated by the shaded areas in Fig. 1 exemplary for the pulse at +0.55 V. Taking the whole range of the period including the base potential makes sure to cover the complete material loss released during the pulse, and over the total dissolution sequence.

Fig. 2 shows the total dissolution currents integrated over all pulses of a sequence for all measured alloys, as function of the Cr, Fe and Mn contents. In the further discussion we will hence reference the observed dissolution pattern of all alloys (see SI for all data) to the binary alloy NiCo, which is at the origin of the plots in Fig. 2, and we discuss the behaviour in terms of adding the other functional elements. For this reference alloy data indicates that Ni and Co dissolve perfectly congruent, in 1:1 ratio, without any passive film formation (see also the respective panel in Fig.).

The principal elements Cr, Mn and Fe that form the axis for the plots in Fig. 2 have a significant influence on the dissolution behaviour, and hence presumably on the passive film properties.

In detail, Fig. 2 shows a 3D scatter plot of the dissolution tendency at three representative applied pulse potentials of +0.5 V, +1.0 V and +1.5 V, respectively, recorded in 1.0 mM NaCl neutral solution. The axes show the composition of Cr, Fe and Mn alloyed with Ni and Co or Ni only. Each plane displays the alloys containing two out of the three elements of interest (Cr, Fe and Mn) alloyed with Ni. The corners are occupied by the binary alloys NiCr, NiFe, NiMn and NiCo. The size and colour of the spheres in the scatter plot relate to the amount of total dissolution per indicated pulse potential.

The three potentials have been selected according to different sections of material degradation. +0.5 V represents an inital stage, at 1.0 V passivity already broke down (indicated by e.g. starting Cr dissolution seen in and in generally rising current steps in). At +1.5 V almost no passivity is observable. Data for each potential can be summarised as follows:

At +0.5 V: Starting from the NiCo alloy as a reference without Cr, Fe and Mn, both addition of Cr and Fe (Cr and Fe axes) result in lower dissolution rates. In contrast, addition of Mn significantly promotes the dissolution (Mn axis). However, most of the studied alloys show very mild dissolution rates at this potential, particularly on the Cr-Fe plane, where we observe a clear trend of passivity increasing with the rise of Cr and Fe co-mixing level. Alloys containing less than 20% of both Cr and Fe exhibit relatively higher dissolution rates, e.g. NiCo, NBACr5 and NBA600.

Further, when mixing Cr with Mn, we observe a clear increase of dissolution rate with higher Mn content (as shown in the Cr-Mn plane). Here, the increasing of the Cr content does not in general passivate the alloy as can be seen in comparing NiCrMn (33% Cr) and NiCoCrMn (25% Cr), where the former shows a more significant dissolution rate than NiCoCrMn. Additionally, NiCrMn (33% Cr) shows in comparison with NiCoMn (0% Cr) a similar dissolution rate, suggesting that Cr is not functioning effectively as a passive film former in the presence of Mn.

Interestingly, the combination of Fe and Mn (Fe-Mn plane) gives an unexpected high dissolution rate for alloy NiCoFeMn, whereas the similar alloy NiFeMn shows a very mild dissolution rate.

At +1.0 V: For all alloys containing Cr at this polarization, passivity built up by the chromium oxide is expected to deteriorate. This feature can be clearly observed in Supporting Figure, which indicates that the Cr-dissolution rate starts to increase to bulk ratio at increasingly higher potentials.

At this potential most of the alloys on the Cr-Fe plane are showing increasing dissolution rate compared to +0.5 V polarization, with the alloys containing less Cr and Fe exhibiting higher dissolution rates. Mn-containing alloys develop increasing dissolution rates, except for NiFeMn, which still exhibits comparably low dissolution.

For the binary alloys, NiCr starts to show a weakening of its passivity due to the chromium oxide breakdown, while NiFe still remains at an extremely low dissolution rate. As expected, NiMn shows a progressive increase of dissolution rate, and indicates no effective passive film formation.

At +1.5 V:

At this polarization, most of the low or no Cr containing alloys develop very high dissolution rates. Interestingly, even it is well-known that Cr passive layers can break down at this polarization, alloys on the Cr-Fe plane still show significantly lower dis-

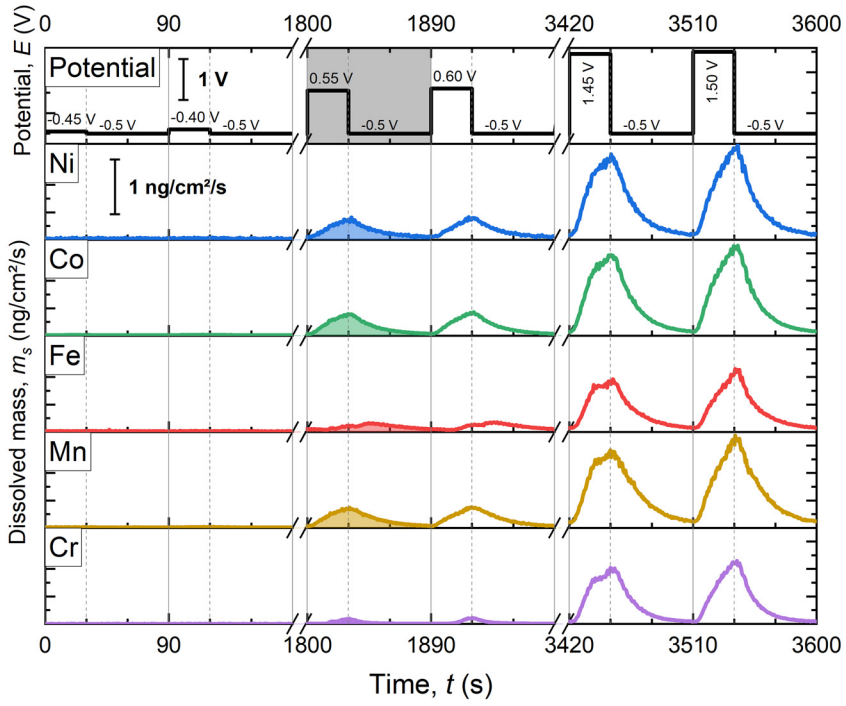

Fig. 1. Detail of normal pulse voltammetry experiment on HEA alloy (NiCoCrFeMn) in neutral 1 mM NaCl solution. Shaded areas indicate exemplarily limits for integration per period. Two periods cut from the beginning, middle and end of the experiment are shown. In the sequence the base potential is -0.5 V and the highest polarization is +1.5 V with the increment per step of +0.05 V.

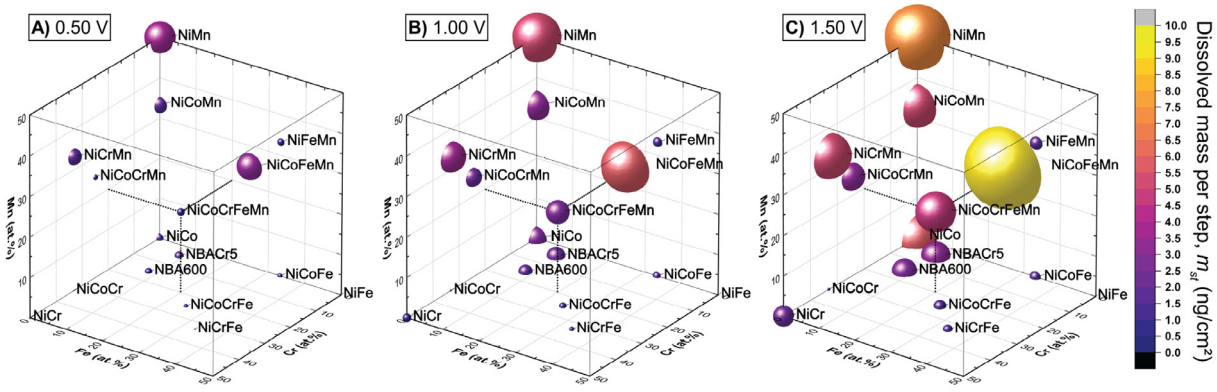

Fig. 2. 3D scatter chart of the ICP-MS detected total dissolved mass of studied alloys at applied potential of A) +0.5 V, B) +1.0 V and C) +1.5 V during normal pulse voltammetry in 1.0 mM NaCl pH 7 electrolyte.

solution rates than most of other Mn-containing alloys. Here, alloy NiCoFeMn again shows the highest dissolution rate among all studied alloys. It is worth mentioning, that the passivity of the NiCoCrFeMn alloy seems balanced by all the alloyed functional materials, which is not as good as Cr-Fe mixed alloys but significantly better than the Mn-alloyed samples and the reference sample (NiCo).

Discussion

Influence of Cr, Fe and Mn

Although Fig. 2 provides us an overview of dissolution tendency of all studied alloys, it is not easy to intuitively extract the influence from individual elements. To visualize the role of the centrally important principal elements in an alloy, a simplified 2D overview with the dissolved mass of tested alloys plotted against atomic ratio of **A)** Cr and **B)** Fe at +0.5 and +1.5 V is shown in Fig. 3.

Here, the studied alloys are grouped into categories according their principal elemental composition: All Mn-containing alloys are highlighted by yellow markers, Cr and Fe co-alloyed substrates have empty markers, and alloys containing solely Fe or Cr (besides Ni and Co) are shown with filled markers. The vertical arrows show the evolution of the mass loss of selected Mn-containing alloys from +0.5 pointing to +1.5 V. Two indicating trend lines (dashed) are plotted to show the trend of dissolved mass as a function of the concentration of the element of interest at +0.5 (thin dash line) and +1.5 V (thick dash line), respectively.

For all Cr-Fe alloyed samples in Fig. 3 A (empty markers), we find a linear relationship between rising Cr concentration and a lowering of dissolution for both the low and high step potentials. As indicated by the dashed trend lines, the slope is related with the magnitude of the anodic polarization applied.

For low polarization of +0.5 V, this linear relationship is applicable to nearly all the Cr-Fe and Cr containing alloys. However, such proportionality seems invalid to NiCr (marked with black filled markers) at high anodic polarization. Here we observe that the mass loss of NiCr at +1.5 V is comparable to NBA600 with a

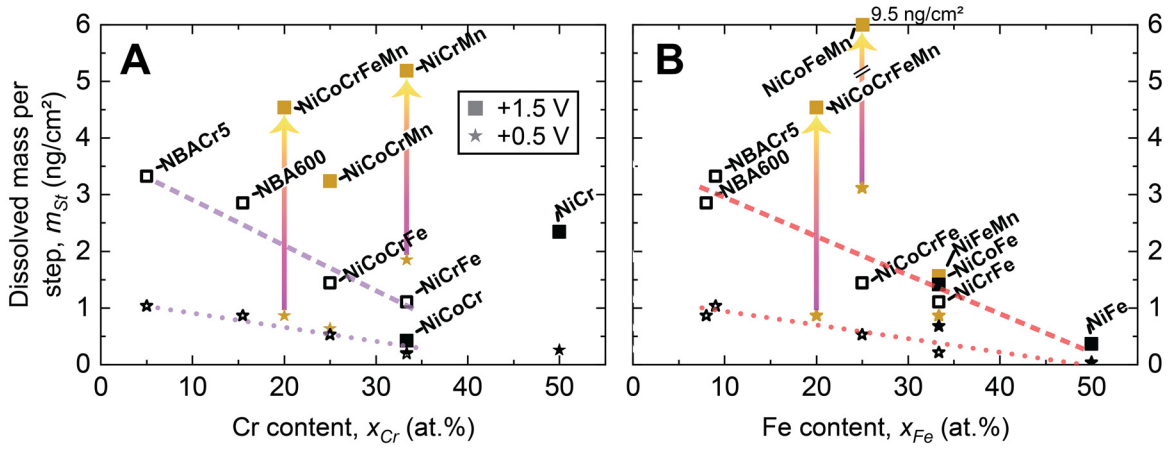

Fig. 3. Influence of Cr A) and Fe B) concentration on the dissolved mass per step for specific potentials (+0.5 (square) and +1.5 V (star)). Trend lines are estimated and extrapolated using only Cr-Fe containing alloys.

Cr-content of 15.5%, suggesting the extra 34.5% Cr is not further stabilizing the alloy. In a sharp contrast, the similar Cr-only containing alloy NiCoCr (also marked in black) exhibits a considerably improved transient passivity. It also shows lower dissolution rates compared to the Cr-Fe containing alloys over the studied polarization range.

Surprisingly, for the NiCoCr the NPV profile shows, that the break-down potential for Cr in this alloy is shifted by +0.25 V towards more anodic potentials compared to the other Cr-Fe containing alloys (see SI). This suggest the formation of a significantly stabilized chromium oxide structure, such as *e.g.* spinel $(NiCo)Cr_2O_4$.

Our results indicate that - without the participation of Fe or Co - Cr itself is not able to form an effective transient passive film at higher potentials. This correlation is in line with the behaviour of pure chromium oxide passive films reported by Tranchida et al. [25] where it exhibits weaker passivity compared to stainless steel at high anodic polarization. Adding Co may increase passivity without the presence of Fe and Mn (see NiCoCr). Again, this is in line with the formation of a thin film of the very stable spinel cobalt chromite ($CoCr_2O_4$), which results in the significant anodic shift of the Cr breakdown potential. It has also been reported in literature that the oxide of NiCoCrFeMn may form a spinel structure [4], which is consistent with the observed anodic stabilization of the oxide in this work.

As can be further seen in Fig. 2, the transient passive film stability is further deteriorated by the addition of Mn (brown markers). Interestingly, the influence of Mn depends on both the applied polarization as well as the co-alloyed metals. For +0.5 V the impairing effect of the Mn is not yet clear for the alloys with only 20–25% Mn, namely NiCoCrFeMn and NiCoCrMn. Here we observe that the dissolution rates of both NiCoCrFeMn and NiCoCrMn are still in accordance with the trend seen for Cr-Fe containing alloys. Among all Cr-containing alloys at this potential, NiCrMn shows the highest dissolution rate.

It clearly pictures the metal-metal interactions across Co, Cr, Fe and Mn, that alloying Cr together with either Co and/or Fe can provide good passivity at +0.5 V polarization whether or not Mn is present. Without the participation of Co or Fe, the passivity of Cr deteriorates even at low polarization with the addition of Mn. At potentials higher than +0.5 V, the passivity imposed by Co, Fe and Cr is significantly deteriorated by Mn (see again yellow square data points in Fig. 3 A).

A similar analysis as a function of the Fe composition is shown in Fig. 3 B, where potential-dependent trend lines for +0.5 (stars) and +1.5 V polarisation (squares) are indicated. Here we again observe a decreasing trend of mass loss in all Cr-Fe containing alloys with the increase of Fe concentration. In addition, most other Cr-free Fe-containing alloys also fit well on these trend lines apart from two Mn containing alloys: NiCoCrFeMn and NiCoFeMn. Our results suggest the formation of a Fe containing passive film lowering dissolution, which shows positive synergy with Cr. As such, data suggests that Fe forms an insoluble layer that limits dissolution at high potentials, where the chromium oxide fails to provide any passivity. This, however, does not imply a general good corrosion resistance, as the insoluble iron oxide is not necessarily forming a well adhering passive film in most cases.

The three studied Mn-Fe containing alloys exhibit in each case a different behaviour. Firstly, NiFeMn shows exactly the same dissolution trend as other Fe-containing alloys for both low and high anodic polarization. Secondly, NiCoFeMn shows completely opposite behaviour compared to NiFeMn, which exhibits the highest dissolution rate at +0.5 V among all studied samples, and further develops to 9.5 ng/cm^2 at +1.5 V. Interestingly, the dissolution behaviour of NiCoCrFeMn exhibits a potential dependency similar to NiFeMn at +0.5 V, but then for +1.5 V shows significant higher mass dissolved.

In a short summary, we conclude for the influence of Cr and Fe a strong correlation of dissolution rate and iron content, while for Cr such a correlation is only limited to the Cr-Fe-containing alloys. Addition of Mn in general deteriorates the passivity in most of Cr related alloys (Fig. 3 A) at high polarization, as it is expected since Mn itself is known to form only weak and porous oxides [26]. However we did not find a direct Mn-Fe correlation.

Fe dissolution profiles

Although the amount of total dissolved mass is a good indicator for the transient passivity of the alloys, it can not clearly explain the difference in passivation mechanisms between alloys. Scaling the total dissolved mass over a whole sequence down to individual pulses (as indicated in Fig. 1, shaded areas), we found a clear change in dissolution patterns across all studied alloys between the anodic step pulse and reconditioning potentials. During the period of a single step, the majority of the integrated mass is collected from the dissolution during the applied step potential, which is later labelled as "anodic peak". Switching from the step potential back to the reconditioning potential, most of the cases show a logarithmic decay profile due to the diffusion broadening during the transportation. However, the dissolution profiles clearly indicate that particular cases (Ni-Cr containing alloys as e.g. NiCoCrFe, NiCoCrFeMn, NiCrFe) exhibit a clear active Fe dissolution during the recondition phase, which is labelled as "cathodic peak". In ad-

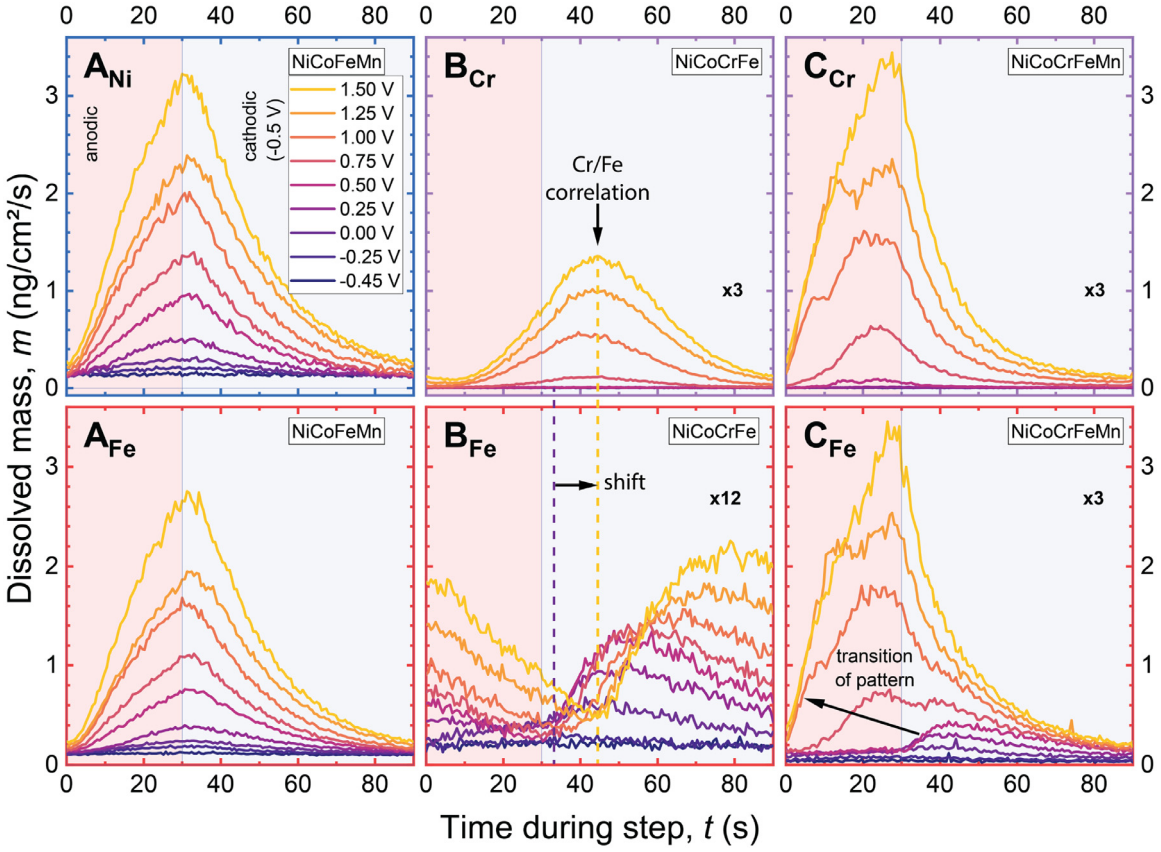

Fig. 4. Elemental dissolution behaviour of Fe (red outline) comparing with Ni (blue outline) and Cr (purple outline) in NPV sequence for (A) NiCoFeMn, (B) NiCoCrFe and (C) NiCoCrFeMn stacked with selected step potentials. Anodic polarization (red shading) at rising potentials is followed by reconditioning potential at -0.5 V (cathodic polarization).

dition, this cathodic dissolution peak shows a pronounced shift in response to the level of the previously applied anodic polarization, likely due to kinetic inhibition of the dissolution (noted as shifted in Fig. 4).

Fig. 4 selectively displays stacked dissolution profiles for picked NPV pulse periods of elements of interest to correlate the elemental mass loss with applied step polarizations. Here we particularly discuss three Fe containing MPEAs, namely **A)** NiCoFeMn, **B)** NiCoCrFe and **C)** NiCoCrFeMn, which characterise typical cases of dissolution profiles found for the entirety of all alloys.

Panel A_{Ni} exemplary shows Ni-dissolution from NiCoFeMn to demonstrate the typical anodic peak profile, which generally applies for all other elements in this alloy, including Fe, as shown in Fig. 4 panel A_{Fe}.

In contrast a pronounced cathodic peak profile is observed for NiCoCrFe in Fig. 4 B_{Fe}, with a very steep increase of the Fe-dissolution rate upon application of the recondition potential of -0.5 V, indicative of an oxide stripping at negative potentials.

Further, in panel Fig. 4 B_{Cr} we also notice that the dissolution profile of Cr in NiCoCrFe increases with increasing anodic polarization. No significant Cr dissolution is observed below 0.5 V. Further, the evolving profile at higher polarizations does not directly correlate with switching from anodic to cathodic. In contrast, the measured maximum dissolution current, indicative of the halt of Cr-dissolution, occurs around 10 s after polarization switching. At the same time, this correlates (indicated by the dashed line) with the, now shifted, initiation of the cathodic iron dissolution.

This suggests a moderated/delayed electrochemical dissolution of Fe, likely across a stable oxide of Cr and Fe, that is only dissolving cathodically. Hence, e.g. the onset Fe dissolution is expected to occur across this stable oxide by travel via vacancies or ion conduction, driven by the high field gradient. This results in a gradient of concentration in the oxide film with increased Fe at the oxide|liquid interface while Cr is enriched at the metal|oxide interface. In particular, the diffusivities differ for each metal, following a trend of D(Mn)>D(Fe)>D(Cr)>D(Ni) [27]. This can further contribute to establishing gradients in the oxide layer, including the formation of complex duplex layered oxides.

In contrast, for the Mn-containing alloy NiCoCrFeMn the Fe dissolution profile shown in Fig. 4 C_{Fe} exhibits both, a cathodic dissolution after application of low potentials while it transitions into a clearly anodic dissolution for Cr and Fe above 0.5 V. This suggest that Mn significantly deteriorates the passive film quality of the Fe/Cr layer, indicated by a strong anodic dissolution at potentials above 0.5 V. This is an indicator for a dissolution mediating or promoting effect of Mn by *e.g.* catalysing the formation of soluble chromates and prevention of the formation of stable oxides. Further, ToF-SIMS data of oxide formation on NiCoCrFeMn[28] indicated a concurrent evolution of Mn and Cr oxides across the layer. In essence, the significant thermodynamic instability of $Mn_2O_3 - Cr_2O_3$ miscibility could also enhance [29] the instability of the these oxides in the presence of Mn.

Precisely, participation of Mn effectively changes the Fe dissolution pattern from cathodic to anodic dissolution.

In addition, Cr simultaneously breaks down with Fe under high polarisation, rendering the passivating elements electrochemically unstable, due to the presence of Mn.

As such, this data strongly suggests that the electrochemical pathway for the formation of an insoluble Cr-Fe passive oxide film is converted into active Cr dissolution. For a more detailed char-

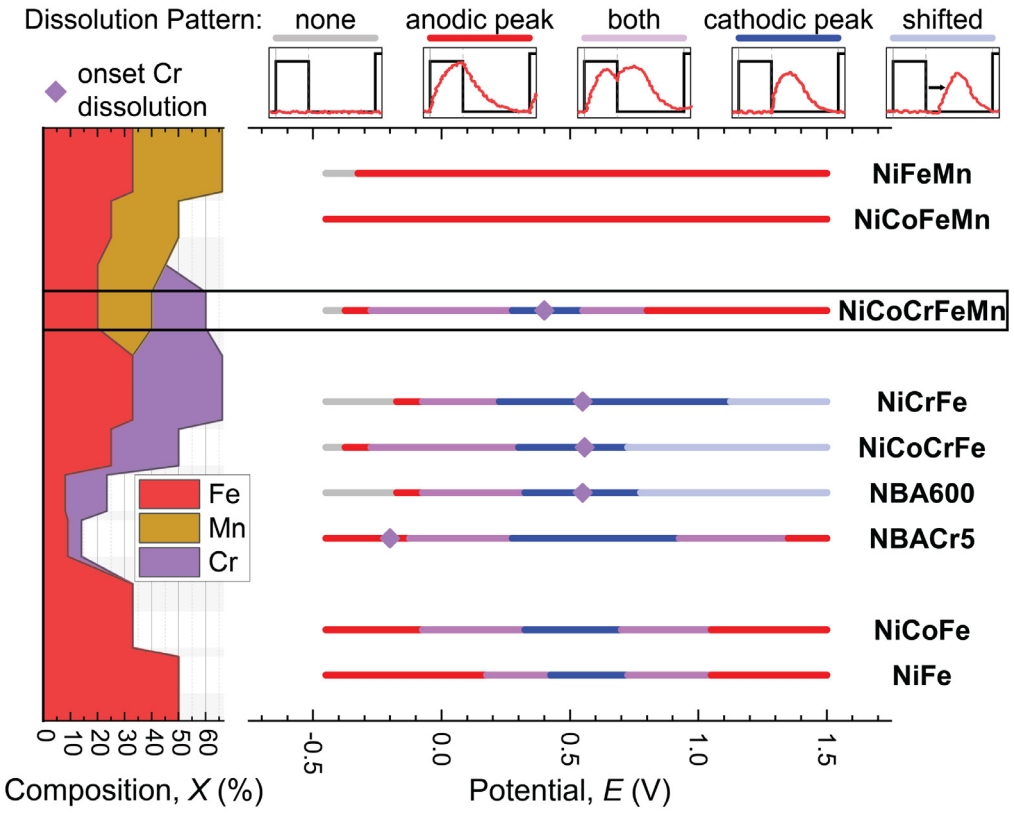

Fig. 5. Distribution of the various Fe dissolution phenomena observed over the step potential range of -0.5 to +1.5 V during NPV, sorted by the presence of Cr and Mn. Anodic and cathodic peak indicate a clear onset of dissolution with the sudden change of potential towards more positive or negative potentials, respectively. The label 'both' is assigned for pulses where anodically and cathodically dissolved Fe could be detected simultaneously. Label 'none' indicate that no dissolution is detected. The left graph shows the composition of the alloys in Fe, Cr and Mn with Ni and/or Co co-alloyed.

acterisation of the thin film chemistry elaborated highly sensitive *in situ* would be needed [30,31].

For a better overview we summarise in Fig. 5 the observed Fe dissolution patterns of all studied alloys sorted by categories. Here, we assigned each Fe dissolution profile to one of five patterns labelled with different colours as shown at the top panel. The main line-chart displays the patterns found at each applied step potential over the whole studied polarization range. The graph on the left shows the composition of Fe, Cr and Mn with Ni/NiCo as background matrix of the studied alloys.

The alloys on the top containing Mn only, besides Fe and Ni/Co, exhibit solely "anodic peak" dissolution of Fe over the whole range of applied potential. This indicates no passive film formation. With the presence of Cr (i.e. in NiCoCrFeMn), the Fe dissolution pattern at a given range of step polarization is altered from pure "anodic peak" to "cathodic peak". The first transition from anodic to cathodic peak is around -0.2 V, where the dissolution rate is significantly reduced compared to NiCoFeMn in the same region. This indicates a clear Cr dependent passivity in low polarization being introduced to the Fe-Mn containing alloy. However, the break-down of Cr at higher anodic polarization triggers the second transition from cathodic back to the anodic peak around +0.5 V, where the dissolution rate becomes higher again. Hence, in the presence of Mn, the window of passivity is decreased significantly.

In the absence of Mn, and in the presence of both Cr and Fe, i.e. NiCrFe, NiCoCrFe and NBA600, we find a large window of passivity (cathodic peak), with a significant kinetic stabilisation upon application of higher potentials (shifted cathodic dissolution).

If the Cr content is below 10%, as for the NBACr5, the passive film is less stable, and also transitions into a purely anodic (i.e. unprotected) dissolution at high potentials above 1.3 V.

Further, if no Cr is present at all, the Fe induced oxide film is less pronounced and above 1.0 V anodic dissolution with no passivity is observed.

In summary, this confirms the synergistic stabilising effect of Fe and Cr in a passive film. In contrast, Mn can completely eradicate its anodic stability over a large range of potentials. Cr can only stabilise a Mn containing alloy at low potentials before Cr dissolution becomes apparent.

Conclusion

By systematically combining a material library of equimolar binary up to quintenary alloys of Ni, Co, Cr, Fe and Mn, we have successfully identified the influence of individual principal elements on the electrochemical properties and corrosion resistivity of alloys. In this work we provide a detailed mechanistic understanding of the qualitatively well-known effects of Mn on passive film stability, as well as Fe/Cr synergies in the passive region. Among the five studied principal elements Cr, Mn and Fe play the mechanistic roles of the individual elements can be summarized as follows:

- Cr alone is not sufficient for achieving a good corrosion resistivity. Fe and Cr exhibit a synergistic effect on the passivation behaviour, expressed by a low dissolution rate (NiCoCrFe, NiCrFe) of both elements.
- Mechanistic insights into passivation confirm an increased stability of Fe/Cr oxides at high potentials. This suggests on the one hand a stable passive film chemistry through which Fe dissolution is moderated and delayed if no Mn is present. This results in a gradient of iron with an increased concentration at the oxide|liquid interface, and delayed Cr dissolution during cathodic dissolution. Mn on the other hand can catalyse the dis-

solution of Fe/Cr oxide and prevents the formation of stable oxides.
- NiCoCr is exceptionally stable and forms stable transient Cr passive films up to +1.2 V, which may be related to a spinel formation.
- However, a high chromium content in itself does not necessarily lead to a stable transient passive film. Mn triggers a breakdown of Cr induced passivity. Cr can only form a protecting passive film at potentials below +0.3 V.

The utilisation of NPV in an ICP-flow cell provides a direct view into the passivity film window and passive film chemistry of a material. The established approach will prove useful for the characterisation of other alloys and material libraries. The method, when applied to a variety of material classes has the potential to provide insightful data sets also for machine learning algorithms.

Materials and methods

Chemicals and Sample preparation

All the alloys were designed equimolarly and synthesized by vacuum-arc melting with a water-cooled bowl mould. These alloys were NiMn, NiCo, NiFe, NiCr, NiCrMn, NiCrFe, NiMnFe, NiCoFe, NiCoCr, NiCoMn, NiCoCrFe, NiCoFeMn, NiCoCrMn, NiCoCrFeMn. All the alloys were flipped and remelted at least four times, and finally remelted into rectangular shape in a water-cooled rectangular mould. Homogenization treatment was conducted at 1100 ℃ for 6 h followed by water-quenching in order to get rid of interdendritic structure. However, homogenization treatment of NiMn alloy was conducted at 1000 ℃ because its melting point is below 1100 ℃ [32]. Then, all the alloys except NiMn alloy were cold-rolled to 70% and recrystallized at 1100 ℃ for 1 h followed by water-quenching to get uniform grain size around 100 to 200 μm. Cold-rolling cannot be conducted to NiMn alloy because of the complex second phase precipitation. [32]

Eventually, all the alloys were line-cut into small samples of dimension $10 \times 10 \times 1$ mm for experiment. All equimolar alloys are reported [33] to be *fcc* single phased, with the exception of the multi phased NiMn, NiCr, and NiCrMn.

Alloy NBA600 was obtained from VDM-Metals, NBACr5 was provided by Hauke Springer (MPI f. Eisenforschung, Düsseldorf). Metals were ground prior experiment with P2500 sand paper and polished with diamond paste down to 0.1 μm, then cleaned in ethanol in an ultrasonic bath and then used without any further preconditioning.

Inductively coupled plasma mass spectrometry

Measurements are carried out with an Agilent 7900 ICP-MS (Agilent Technologies, US), a collision cell with 5 mL/min flow of helium as cell gas is used. Calibration is performed with multi-element standards (Inorganic Ventures, US). For ICP-MS, downstream of the electrochemical cell, the analyte is mixed with internal standard solution containing Gallium. Electrochemical experiments are conducted in a home-built flow cell out of PEEK and PTFE [23], see also Fig. S1. The exposed electrode area is circular and sealed with a 3 mm inner diameter O-ring. Prior each experiment the electrolyte solution was enriched in dissolved oxygen by purging with compressed and filtered air for at least 30 minutes. The maximum total mass dissolved over the whole experiment in this study is typically at most between 5 and 30% of a metal monolayer, which indicates negligible overall dissolution during this test sequence. As such, this provides us a mean to study the initial quality of a transient passive film formed on the range of studied MPEAs. In addition, the low dissolution rate also prevents any side reactions such as increased dissolution under the O-ring of the used cell.

Electrochemistry

A Biologic VSP-300 potentiostat (Biologic, France) or a PalmSens 4 (PalmSens BV, NL) is used for electrochemical measurements. All electrochemical experiments are performed with a Ag|AgCl-Electrode (in 3 M KCl, Multichannel Systems, DE) as reference electrode, all potentials shown in this manuscript are referenced against Ag|AgCl.

The counter electrode is made from platinum. Normal Pulse Voltammetry was conducted starting from a base potential of -0.5 V to an upper potential of +1.5 V. Pulses with a step height of 50 mV and a pulse width of 30 s are applied in periods of 90 s.

Data availability

The data that support the findings of this study are available on reasonable request from the corresponding authors, M.V. and H.-W.C.

Declaration of Competing Interest

The authors declare that they have no known competing financial interests or personal relationships that could have appeared to influence the work reported in this paper.

Acknowledgments

The authors thank the European Research Council for the support (ERC-StG Grant No. 677663). The authors appreciate financial support by the High Entropy Materials Center from The Featured Areas Research Center Program within the framework of the Higher Education Sprout Project by the Ministry of Education (MOE) and the Project MOST 108-3017-F-007-002 by the Ministry of Science and Technology (MOST) in Taiwan.

Supplementary material

Supplementary material associated with this article can be found, in the online version, at 10.1016/j.electacta.2021.139804

References

[1] J.-W. Yeh, S.-K. Chen, S.-J. Lin, J.-Y. Gan, T.-S. Chin, T.-T. Shun, C.-H. Tsau, S.-Y. Chang, Nanostructured high-entropy alloys with multiple principal elements: novel alloy design concepts and outcomes, Adv. Eng. Mater. 6 (5) (2004) 299–303, doi:10.1002/adem.200300567.
[2] C.-Y. Cheng, Y.-C. Yang, Y.-Z. Zhong, Y.-Y. Chen, T. Hsu, J.-W. Yeh, Physical metallurgy of concentrated solid solutions from low-entropy to high-entropy alloys, Curr. Opin. Solid State Mater. Sci. 21 (6) (2017) 299–311, doi:10.1016/j.cossms.2017.09.002. https://linkinghub.elsevier.com/retrieve/pii/S1359028617300591
[3] Y. Li, A. Savan, A. Kostka, H. Stein, A. Ludwig, Accelerated atomic-scale exploration of phase evolution in compositionally complex materials, Mater. Horizons 5 (1) (2018) 86–92.
[4] J. Dąbrowa, M. Stygar, A. Mikuła, A. Knapik, K. Mroczka, W. Tejchman, M. Danielewski, M. Martin, Synthesis and microstructure of the (Co, Cr, Fe, Mn, Ni) 3o4 high entropy oxide characterized by spinel structure, Mater. Lett. 216 (2018) 32–36.
[5] C. Schwanke, H.S. Stein, L. Xi, K. Sliozberg, W. Schuhmann, A. Ludwig, K.M. Lange, Correlating oxygen evolution catalysts activity and electronic structure by a high-throughput investigation of $Ni_1 - yzFe_yCr_zO_x$, Sci. Rep. 7 (1) (2017) 1–7.
[6] A. Sarkar, L. Velasco, D. Wang, Q. Wang, G. Talasila, L. de Biasi, C. Kübel, T. Brezesinski, S.S. Bhattacharya, H. Hahn, et al., High entropy oxides for reversible energy storage, Nat. Commun. 9 (1) (2018) 1–9.
[7] Y. Yuan, Y. Wu, H. Luo, Z. Wang, X. Liang, Z. Yang, H. Wang, X. Liu, Z. Lu, Superconducting Ti15Zr15Nb35Ta35 high-entropy alloy with intermediate electron-phonon coupling, Front. Mater. 5 (2018), doi:10.3389/fmats.2018.00072.
[8] J.-W. Yeh, Alloy design strategies and future trends in high-entropy alloys, JOM 65 (12) (2013) 1759–1771.

[9] J.R. Hayes, J.J. Gray, A.W. Szmodis, C.A. Orme, Influence of chromium and molybdenum on the corrosion of nickel-based alloys, Corrosion 62 (6) (2006) 491–500, doi:10.5006/1.3279907. http://corrosionjournal.org/doi/10.5006/1.3279907
[10] A.C. Lloyd, J.J. Noël, S. McIntyre, D.W. Shoesmith, Cr, Mo and W alloying additions in Ni and their effect on passivity, Electrochim. Acta 49 (17-18) (2004) 3015–3027, doi:10.1016/j.electacta.2004.01.061. https://linkinghub.elsevier.com/retrieve/pii/S0013468604002749
[11] N. Ebrahimi, P. Jakupi, J.J. Noël, D.W. Shoesmith, The role of alloying elements on the crevice corrosion behavior of Ni-Cr-Mo alloys, Corrosion 71 (12) (2015) 1441–1451, doi:10.5006/1848.
[12] S.Y. Persaud, R.C. Newman, A review of oxidation phenomena in Ni alloys exposed to hydrogenated steam below 500°C, Corrosion 72 (7) (2016) 881–896, doi:10.5006/1957. http://corrosionjournal.org/doi/10.5006/1957
[13] Y.Y. Chen, T. Duval, U.D. Hung, J.W. Yeh, H.C. Shih, Microstructure and electrochemical properties of high entropy alloys—a comparison with type-304 stainless steel, Corros. Sci. 47 (9) (2005) 2257–2279, doi:10.1016/j.corsci.2004.11.008. https://linkinghub.elsevier.com/retrieve/pii/S0010938X04003567
[14] K.-Y. Tsai, M.-H. Tsai, J.-W. Yeh, Sluggish diffusion in Co-Cr-Fe-Mn-Ni high-entropy alloys, Acta Mater. 61 (13) (2013) 4887–4897.
[15] Y. Zhang, K. Jin, H. Xue, C. Lu, R.J. Olsen, L.K. Beland, M.W. Ullah, S. Zhao, H. Bei, D.S. Aidhy, G.D. Samolyuk, L. Wang, M. Caro, A. Caro, G.M. Stocks, B.C. Larson, I.M. Robertson, A.A. Correa, W.J. Weber, Influence of chemical disorder on energy dissipation and defect evolution in advanced alloys, J. Mater. Res. 31 (16) (2016) 2363–2375, doi:10.1557/jmr.2016.269.
[16] Q. Ye, K. Feng, Z. Li, F. Lu, R. Li, J. Huang, Y. Wu, Microstructure and corrosion properties of CrMnFeCoNi high entropy alloy coating, Appl. Surf. Sci. 396 (2017) 1420–1426, doi:10.1016/j.apsusc.2016.11.176.
[17] Z. Han, W. Ren, J. Yang, A. Tian, Y. Du, G. Liu, R. Wei, G. Zhang, Y. Chen, The corrosion behavior of ultra-fine grained CoNiFeCrMn high-entropy alloys, J. Alloy. Compd. 816 (2020) 152583.
[18] A.M. Panindre, Y. Khalifa, C.D. Taylor, G.S. Frankel, Corrosion of Ni-Fe-Cr-Mo-W-X multi-principal element alloys, J. Electrochem. Soc. 168 (3) (2021) 031513, doi:10.1149/1945-7111/abeaef.
[19] K.H. Kim, S.H. Lee, N.D. Nam, J.G. Kim, Effect of cobalt on the corrosion resistance of low alloy steel in sulfuric acid solution, Corros. Sci. 53 (11) (2011) 3576–3587, doi:10.1016/j.corsci.2011.07.001.
[20] N. Birbilis, S. Choudhary, J.R. Scully, M.L. Taheri, A perspective on corrosion of multi-principal element alloys, NPJ Mater. Degrad. 5 (1) (2021), doi:10.1038/s41529-021-00163-8.
[21] H. Stein, M. Suta, J. George, Die Materialsynthesemaschine, Nachr. aus der Chem. 68 (12) (2020) 66–69, doi:10.1002/nadc.20204096061.
[22] E. Soedarmadji, H.S. Stein, S.K. Suram, D. Guevarra, J.M. Gregoire, Tracking materials science data lineage to manage millions of materials experiments and analyses, Npj Comput. Mater. 5 (1) (2019), doi:10.1038/s41524-019-0216-x.
[23] D. Dworschak, C. Brunnhofer, M. Valtiner, Photocorrosion of ZnO single crystals during electrochemical water splitting, ACS Appl. Mater. Interfaces 12 (46) (2020) 51530–51536, doi:10.1021/acsami.0c15508.
[24] K. Ogle, S. Weber, Anodic dissolution of 304 stainless steel using atomic emission spectroelectrochemistry, J. Electrochem. Soc. 147 (5) (2000) 1770–1780, doi:10.1149/1.1393433. http://jes.ecsdl.org/content/147/5/1770
[25] G. Tranchida, M. Clesi, F. Di Franco, F. Di Quarto, M. Santamaria, Electronic properties and corrosion resistance of passive films on austenitic and duplex stainless steels, Electrochim. Acta 273 (2018) 412–423, doi:10.1016/j.electacta.2018.04.058.
[26] K. Park, H. Kwon, Effects of Mn on the localized corrosion behavior of Fe–18Cr alloys, Electrochim. Acta 55 (9) (2010) 3421–3427, doi:10.1016/j.electacta.2010.01.006.
[27] A.Y. Gerard, J. Han, S.J. McDonnell, K. Ogle, E.J. Kautz, D.K. Schreiber, P. Lu, J.E. Saal, G.S. Frankel, J.R. Scully, Aqueous passivation of multi-principal element alloy Ni38fe20cr22mn10co10: usssnexpected high Cr enrichment within the passive film, Acta Mater. 198 (2020) 121–133, doi:10.1016/j.actamat.2020.07.024.
[28] L. Wang, D. Mercier, S. Zanna, A. Seyeux, M. Laurent-Brocq, L. Perrire, I. Guillot, P. Marcus, Study of the surface oxides and corrosion behaviour of an equiatomic cocrfemnni high entropy alloy by xps and tof-sims, Corros. Sci. 167 (2020) 108507, doi:10.1016/j.corsci.2020.108507.
[29] S. Fajardo, I. Llorente, J.A. Jimnez, J.M. Bastidas, D.M. Bastidas, Effect of Mn additions on the corrosion behaviour of twip Fe-Mn-Al-Si austenitic steel in chloride solution, Corros. Sci. 154 (2019) 246–253, doi:10.1016/j.corsci.2019.04.026.
[30] F.U. Renner, A. Stierle, H. Dosch, D.M. Kolb, T.-L. Lee, J. Zegenhagen, Initial corrosion observed on the atomic scale, Nature 439 (7077) (2006) 707–710.
[31] F. Reikowski, F. Maroun, I. Pacheco, T. Wiegmann, P. Allongue, J. Stettner, O.M. Magnussen, Operando surface x-ray diffraction studies of structurally defined Co_3O_4 and CoOOH thin films during oxygen evolution, ACS Catal. 9 (5) (2019) 3811–3821.
[32] ASM handbook : 3. Alloy phase diagrams, American Society for Metals (Ed.), Materials Park, Ohio : ASM International, Materials Park, Ohio, 1992. https://permalink.catalogplus.tuwien.at/AC00569357
[33] Z. Wu, H. Bei, F. Otto, G.M. Pharr, E.P. George, Recovery, recrystallization, grain growth and phase stability of a family of fcc-structured multi-component equiatomic solid solution alloys, Intermetallics 46 (2014) 131–140, doi:10.1016/j.intermet.2013.10.024.